Influence of substrate temperature on delafossite $CuFeO_2$ films synthesized by reactive magnetron sputtering

N. Ziani[a], E. Aubry[b], N. Martin[c], L. Hirsinger[c], A. Billard[b], P. Briois[b], M. S. Belkaid[a], and M. Arab Pour Yazdi[b]

[a] Laboratory of Advanced Technologies of Genie Electrics (LATAGE), Mouloud Mammeri University (UMMTO), 15000 TiziOzou, Algeria

[b] Institut FEMTO-ST, UMR 6174 CNRS, UTBM, Univ. Bourgogne Franche-Comté, Rue Ernest Thierry Mieg, Site de Montbéliard, 90010 Belfort cedex, France

[c] Institut FEMTO-ST, UMR 6174, CNRS, Univ. Bourgogne Franche-Comté, 15B, Avenue des Montboucons, 25030 Besançon, France

Abstract

Delafossite $CuFeO_2$ films have been synthesized by reactive magnetron sputtering at different substrate temperatures from 380 up to 550 °C. The films adopt the rhombohedral structure from 380 to 550 °C. At the highest temperature, the delafossite phase partially dissociates in FCC Cu and Fe_3O_4 magnetite phases. In addition to the average crystallite size increase, a change of the preferential orientation in the out-of-plane direction from the [012] to [006] directions occurs between 460 and 510 °C. Modelling of the optical properties shows the presence of 2 interband transitions in the visible range. The 1st main transition at 1.5 eV is ascribed to the absorption component parallel to the c-axis whereas the 2nd transition (2.10 – 2.26 eV) is related to the absorption component in the (a, b) plane. Both evolutions with temperature of the refractive index (~ 2.5) and absorption coefficient (~ 10^{-3} cm^{-1}) in the infrared suggest the formation of secondary phases having lower oxidation state. The electronic conductivity, dominated by positive charge carrier, varied from 0.01–10 S m^{-1} according to the preferential orientation and to the presence of secondary phases. A very small amount of a short-range ferromagnetic component (magnetization ~ 10 kA m^{-1} at 1.5 T) is clearly observed at room temperature thanks to magnetometry confirming the formation of secondary phases undetected by X-ray diffraction. In addition to depend on the

film orientation, the presence of secondary phases in weak proportion alters the optical and electrical behaviours such as the transmittance in the visible range.

Keywords

Delafossite; reactive sputtering; substrate temperature; TCO

1. Introduction

The iron is an element of non-negligible quantity in the earth crust (representing about 5% in volume which put it after Si and Al) with advantage of its easy recyclability due to its ferromagnetic property. As a result, iron-based materials are still the subject of interest and research despite the fact that they are already widely used. Among them, delafossite $X^{+}Fe^{3+}O_2$ mineral group has a layered structure composed by sheets of linearly coordinated X^{+} cations stacked between distorted FeO_6 octahedrons resulting in $(FeO_2)^{-}$ layer [1]. This distinctive characteristic is responsible of the relatively superior in-plane electrical conductivity compared to that along the c axis [2]. According to the sequence of stacking layers, two polytypes (rhombohedral or hexagonal) exist and exhibit high cell anisotropy (the c parameter being around 6 or 4 times longer than a parameter, respectively). It was demonstrated that the top of the valence and the bottom of the conduction band are mainly constituted by Cu-3d states and by Fe-3d states, respectively, while the O-2p states are hybridized with both states [3][4]. This compound exhibits a multi-band spectral absorption which would be advantageous in solar applications. Furthermore delafossite $CuFeO_2$ compound exhibits semiconducting behaviour [5] with p- or n-type according to the nature of the dopant [1] [2], and it can also be considered as a Mott insulator [6]. In addition to its electrical transport in new regimes, this compound is antiferromagnetic with two reported Néel temperatures at 10.5 and 14 K, which stems from the triangular lattices of Fe^{3+} layers separated by nonmagnetic Cu^{1+} and O^{2-} layers [3][4]. This formation is one of the reasons of antiferromagnetic ordering in the structure [6][7][8] and multiferroic properties [9]. Theoretical investigations on $CuMO_2$ compounds (with M = IIIA, 3d, 4d, 5d, and rare earth elements) have highlighted the functions of the different substructures in the mechanisms of light absorption, charges separation and transport demonstrating that $CuFeO_2$ is suitable for solar applications such as photovoltaic [10]. Some

authors have also studied its thermoelectric [9][11][12] and its photocatalytic properties [4][13][14].

However, the synthesis of the single phase delafossite without impurity is non-trivial because the Cu valency must be maintained at its lowest value (+1) while avoiding the formation of the stable spinel $CuFe_2O_4$ or other binary compounds. Different processes have been used to produce delafossite $CuFeO_2$-based thin films, *e.g.* pulsed laser deposition [7][15], spray pyrolysis [16][17], sol-gel [18][19] or radio-frequency sputtering [20][21][22][23][24]. It can be noted that an elevated substrate temperature or additional annealing step in neutral atmosphere or in primary vacuum is often required to obtain a crystalline structure, meaning that its synthesis without impurity phase is possible only for a limited range of oxygen partial pressures. To overcome the drawbacks intrinsic to the radio-frequency sputtering (lower deposition rate, higher sputtering pressure, tendency to crack the compound target, efficient cooling system, use of impedance matching box, drift of the chemical composition of the synthesized film due to sputtering yield difference), it is proposed to directly synthesize the delafossite compound from Cu and Fe metallic targets using reactive magnetron sputtering on hot substrates. So far, the role of substrate temperature on the structural, optical, electrical and magnetic properties of delafossite $CuFeO_2$ thin films synthesized by reactive magnetron sputtering have not been explored yet. The changes induced by the increase of the deposition temperature on the structural properties regarding the involved phases and their preferential orientation in the out-of-plane direction is first discussed. In addition to depend on the film orientation, the optical and electrical behaviours suggest the presence of secondary phases with decreasing oxidation state with the increase of the deposition temperature. Besides, the magnetic measurements confirmed the presence of ferromagnetic phase related to the increase of reduction conditions with the deposition temperature, which contributes to the observed optical and electrical properties.

2. Material and methods

2.1 Delafossite $CuFeO_2$ films preparation

$CuFeO_2$ thin films, with a chemical concentration Cu/Fe ratio of 1, were deposited by reactive magnetron sputtering of Cu and Fe metallic targets in a Ar and O_2 gas mixture. The sputtering

system consists in a 90 L stainless steel vessel (Alcatel SCM 604) equipped with 2 water-cooled and balanced magnetron targets (Ø 50 mm, thickness 3 mm). Prior the deposition step, a base pressure lower than 10^{-4} Pa was obtained with a turbomolecular pump unit. The iron and copper targets were supplied with a pulsed Advanced Energy Pinnacle^{+} power generator (J_{Fe} = 188-214 A m^{-2}) and a DC Advanced Energy MDX 500 power generator (J_{Cu} = 14 A m^{-2}), respectively, leading to Fe/Cu atomic ratio of 1. The sputtering of ferromagnetic element by conventional magnetron is low and poorly reproducible. It requires a special geometry of the magnetron to ignite and sustain the discharge with an efficient iron sputtering [25], and to increase the reproducibility of the deposition conditions. In addition, the Fe target thickness has been reduced to 1 mm so as to obtain a magnetic field above the targets sufficient to ignite and maintain the discharge. Ar and O_2 gases flow rates were controlled with Brooks flowmeters with D_{Ar} = 100 sccm and D_{O_2} = 10 sccm, respectively. It is noteworthy that the O_2 flow rate is enough to maintain the sputtering process in the compound mode. MKS Baratron gauge was used to measure the total pressure (P_{tot} = 2.2 Pa). Fused silica glass slides were used as substrates (76 x 26 x 1.1 mm^3), and were located on a heating and rotating substrate-holder parallel to the surface target at about 60 mm. The substrate-holder was referenced to ground and its rotation speed was fixed at 60 rpm. The substrate temperature was varied from 380 to 550 °C with a graphite electrical resistance heater placed behind the substrate-holder while keeping constant other deposition parameters.

2.2 $CuFeO_2$ films characterization

The film thickness (fixed at 440 ± 16 nm) was determined from the cross-section observation of the films via a Field Emission Scanning Electron Microscope (FE-SEM JEOL JSM -7800F) and by using spectrophotometry. The structural features of the films were investigated by using a Bruker D8 focus diffractometer (Co $K_{\alpha_{1+2}}$ radiation) equipped with the LynxEye linear detector in a Bragg Brentano configuration (0.02° step). The total optical transmittance and reflectance of the films were measured with a Shimadzu UV-3600 spectrophotometer equipped with ISR-3100 integrating sphere in the range 220–2600 nm. Standard white board $BaSO_4$ was used for the baseline. Optical simulations of the transmittance and reflectance spectra were realized with the SCOUT software to determine some optical properties such as refractive index, absorption coefficient [26]. The electrical conductivity of the films was determined from the sheet resistance measured using conventional four probe method (Jandel system). A detailed study of the electrical

properties was carried out by measuring the charge carrier concentration and mobility by Hall effect in the temperature range 30-200 °C by means of a homemade system based on the van der Pauw method with a magnetic field of 0.8 T perpendicularly applied to the sample surface. Magnetometry measurements in static mode (point by point, 16 kA m^{-1}) were performed with a vibrating sample magnetometer (Microsense model EZ7) at room temperature with a magnetic field (up to ± 1.5 T) applied to the plane of the films. The diamagnetic contribution of the substrate holder was removed from the measured magnetization. The Seebeck coefficient was measured at room temperature by means of a homemade system. For hot and cold sources, copper material was used as superconductor and the temperature of hot source was maintained constant at set point value by hot water circulation inside of hot source (25 °C). The real-time value of temperature was determined with CHY 505 RTD thermometer (Centenary Materials Co. Ltd., Hsin-Chu City, Taiwan) and the difference of potential between hot and cold side of the sample was performed using a frame grabber of National Instrument USB-4065 (Electronic Test Equipment, Cary, NC, USA). The relative Seebeck coefficient α ($\mu V\ K^{-1}$) was calculated by using the following formula:

$$\alpha = - \Delta V/\Delta T \qquad (1)$$

Where ΔV is the potential difference (μV) and ΔT is the temperature difference (K) between hot and cold side of the samples, respectively. In order to find the absolute values of Seebeck coefficient, the absolute Seebeck value for Cu (2 $\mu V\ K^{-1}$ [27]) was subtracted from each measured value. The Seebeck coefficient of each sample was measured 4 times and the errors in the measurement were evaluated to be within 5 %.

3. Results and discussion

3.1 Structural properties

X-ray diffractograms of thin films deposited at different substrate temperatures are shown in Fig. 1. From 380 up to 510 °C, the crystallisation of the delafossite structure in the trigonal $R\bar{3}m$ space group without the presence of secondary phase is observed. At 550 °C, deposition conditions (substrate temperature and O_2 partial pressure) become sufficiently reductive to lead to the partial dissociation of the delafossite structure in semimetallic magnetite Fe_3O_4 and metallic Cu phases.

The use of grazing incidence X-ray diffraction (GIXD) does not underline the occurrence of a specific phase (Fe_3O_4 or Cu) at the sample surface, but rather reveals a fairly homogeneous distribution of the different phases through the film thickness (not shown). If the O_2 partial pressure is high enough to form $CuFeO_2$ compound at low deposition temperature, it can be assumed that, for a constant O_2 partial pressure, the deposition temperature elevation would lead to the reduction of the oxygen content in the growing film (stronger oxygen thermal desorption at more elevated temperature and incapacity to adsorb oxygen during the cooling in vacuum).

Below 510 °C, the delafossite structure exhibits a preferential orientation towards the [012] direction, while higher temperatures lead to a preferential growth along the [00l] axis. Considering spherical crystallites independent on crystallographic directions, their average size has been estimated using the Scherrer's formula from the Full Width at Half Maximum (FWHM) by deconvolution of the 3 most intense peaks corresponding to the (006), (101) and (012) planes (cf. Fig. 2). The instrumental contribution on the line broadening is assumed to be negligible compared to that induced by the size of crystallites. The average crystallite size is stable up to 440 °C, and after deposition at $T_S \geq 460$ °C, while (006) diffraction line was detected, the average crystallite strongly increases for all crystallographic directions. At 550 °C, the crystallite size calculated from the (006) diffraction line is still growing contrary to those measured from other directions. This result is consistent with the observed change in the preferential growth with the deposition temperature. The dislocation density can be approached, for low amount, considering it as the inverse of the square of crystallite size [28]. A decrease of the dislocation density when increasing the temperature during the film growth is thus assumed. Besides, it can be observed that the change in the preferential orientation from [012] to [006] occurs in rather reductive conditions as the deposition temperature increases. It is worth noting that previous observations also reported a preferential orientation along the c-axis direction in rather reductive conditions, e.g. by implementing a crystallization post-treatment of sol-gel films at high temperature (> 600-850 °C) and at O_2 partial pressure of about 10^{-3}–10^{-2} atm [19]. Other authors observed it during the post-treatment of radiofrequency sputtered $CuFeO_2$ films in a primary vacuum at 450 °C as confirmed by the additional crystallization of metal Cu and spinel Fe_3O_4 phases [29].

3.2 Optical properties

Transmittance and reflectance spectra are displayed in Fig. 3. Transmittance spectra exhibit interference fringes in the near infrared region with a steep fall of the transmittance at around 860 nm corresponding to optical absorption by interband electronic transitions. It is noteworthy that the region of the transmittance fall is more abrupt compared to previous studies [16][18][21]. Indeed, some authors observed a progressive decay of the transmittance through the visible range [19][23]. In our case, the transmittance drops from 60 to 5 % through only 150 nm, whereas the same loss was reported through 550 nm [19][23][30]. This corresponds to a poor transparency of delafossite films (only about a few percent and up to 30 % transmittance loss at 420 nm). The average transmittance in the visible range progressively decreases when increasing the deposition temperature to become fully opaque at 550 °C due to the crystallization of magnetite and copper phases (Table 1) [31]. Optical properties cannot be determined with our used methods due to their strong absorbance and reflectance in the studied wavelength.

The absorption coefficient spectrum $\alpha(\lambda)$ was determined from transmittance and reflectance spectra using three different methods. For the first one, the simplified absorption coefficient was calculated from the equation below :

$$\alpha(\lambda)=\frac{1}{t}\ln\left(\frac{(1-R(\lambda))}{T(\lambda)}\right) \qquad (2)$$

Where t is the thickness in cm, $R(\lambda)$ and $T(\lambda)$ are the reflectance and transmittance spectra, respectively. The second method implies the simulation of transmittance and reflectance spectra, by implementing dispersion models. In the first one, designed hereafter by "Cauchy", the refractive index n and the extinction coefficient k were calculated by using the well-known empirical Cauchy model. It should be specified that this model is suitable for low absorption domain (i.e., $\lambda > 1000$ nm in our case):

$$n(\lambda)=A+\frac{B}{\lambda^2}+\frac{C}{\lambda^4} \qquad (3)$$

$$k(\lambda)=D+\frac{E}{\lambda^2}+\frac{F}{\lambda^4} \qquad (4)$$

where A, B, C, D, E, and F are constants. A more sophisticated dispersion model taking into account the strong optical absorption located around 750 nm was also used (Fig. 3). The optical absorption was then modelled with the so-called O'Leary-Johnson-Lim (OJL) model valuable for

interband electronic transitions assuming that tail states exponentially decay into the band gap [32]. Considering the multi-band response of the $CuFeO_2$ material, it is admitted that 3 mains electronic transitions at 1.15, 2.03 and 3.35 eV strongly influence the optical properties [3]. However, only two OJL transitions were necessary to achieve a satisfactory fit of transmittance and reflectance spectra in agreement with a previous study [33], and also with the abrupt fall of the transmittance. In the infrared range where the absorption of light is related to the free charges, a simple Drude model was also introduced to contribute to the dielectric dispersion. No roughness surface or interface was used in this model. The deviation (mean square difference between simulated and measured data) was less than 10^{-4} for the transmittance part and less than 6×10^{-4} for the reflectance part. The higher deviation for the reflectance part is ascribed to the $BaSO_4$ absorption bands from the integration sphere which alter the reflectance spectra in the near infrared range. This dispersion model is named "OJL" in the rest of the study.

Fig. 4 shows the spectral dependency of the absorption coefficient. Far from the absorption edge, the three methods lead to fairly similar results, namely an increase of the deposition temperature gradually degrades the near infrared absorption. This could be related to the absorption of free charge carrier, in which the promotion of already excited charge carrier to an unoccuped state inside the same band (intraband absorption) occurs. Considering the Drude model which reports the charge carrier transport properties due to intraband transition in a metallic solid, the absorption coefficient related to the imagery part of the dielectric constant is then proportional to the charge carrier concentration [34]:

$$\varepsilon_1 = \varepsilon_{opt}\left(1 - \frac{\omega_p^2\tau^2}{1+\omega^2\tau^2}\right) \qquad (5)$$

$$\varepsilon_2 = \frac{\varepsilon_{opt}\omega_p^2\tau}{\omega\left(1+\omega^2\tau^2\right)} \qquad (6)$$

$$\omega_P = \sqrt{\frac{Ne^2}{m\varepsilon_0}} \qquad (7)$$

$$\alpha_{\text{free charge carrier}} = \frac{Ne^2}{m\varepsilon_0 nc\tau\omega^2} \qquad (8)$$

with ε_1, ε_2 are the real and imaginary parts of the dielectric function, respectively, ε_{opt} the dielectric constant far from absorption edge (= n^2 in the transparent region), ω the pulsation (s^{-1}), ω_P the

plasma pulsation (s^{-1}), τ lifetime of charge carrier (s), N the quantity of the charge carrier (m^{-3}), e the elementary charge, m the effective mass (kg), and ε_0 the vacuum permettivity. A decrease of the infrared absorption would therefore be linked to that of the charge carrier concentration. Besides, the presence of a secondary phase absorbing infrared in increasing proportion with the deposition temperature would also explained the decay of the absortion coefficient in this range. For wavelengths lower than 1000 nm, the "Cauchy" model is no more valid. The graphical method for the determination of the absorption coefficient still remains relatively consistent in the medium absorption range (λ < 800 nm), while a slight discrepency in the absorption coefficient can be observed in the strong absorption range (λ < 540 nm) due to the addition of a 2^{nd} OJL transition. In this range, the absorption coefficient increases up to 10^5 cm^{-1} for the films deposited at 380 and 440 °C and becomes even larger for higher deposited temperatures. The strong optical absorption at λ < 800 nm is consistent with previous article [4], in which the authors observed similarly strong absorption, while it started at 1000 nm. It was ascribed to the direct transition O-p_z → Fe-d_{xz}, -d_{z2} at 1.55 eV (O-2p → Fe-3d) with the possible contribution of the indirect transition O-p_x, -p_y → Fe-d_{xy}, -d_{xz}, -d_{yz}, -d_{x2-y2}, -d_{z2} at 1.54 eV.

Spectral dependancies of the refractive index, determined by "Cauchy" and "OJL" models, are presented in Fig. 5. Far from the absorption edge, the refractive index lies between 2.4 and 2.6, with an order of magnitude consistent with the extracted values from ellipsometric spectroscopy [30]. Refractive index follows the same trend with the deposition temperature up to 1000 nm, wavelength for which the "Cauchy" model is no more valid. The measured refractive index in infrared range is affected by the presence of other phases. As a first approximation, the measured refractive index is proportionnal to the volume of the relative phases. Based on our previous assumption, on which oxygen content would be affected by the temperature deposition, a progressive decrease of the refractive index would then be expected with the deposition temperature elevation. In previous study dealing with the annealing conditions of sputtered $CuFeO_2$ films [35], it was observed that a slight enhancement of the reductive conditions (increase of annealing temperature in primary vacuum) leads to the formation of Cu_2O and Fe_2O_3 phases from rhombohedral delafossite phase, while with even more reductive conditions (same temperature range combined with secondary vacuum) only Cu and Fe_3O_4 phases crystallize. Refractive indices of Cu_2O and Fe_2O_3 are 2.6 to 2.27 and 2.78 to 2.66 in the infrared range (1000 to 2600 nm,

respectively) [36], and the refractive indices of metallic Cu included from 0.46 to 1.09 and of the spinel Fe_3O_4 are included from 2.13 to 2.85 at 1000 to 2600 nm, respectively. [36]. The formation of phases with relative high refractive index such as Fe_2O_3 hematite and Cu_2O would explain the observed increase of the refractive index at 460 °C. It is noteworthy that the bandgap energy of Fe_2O_3 (~ 600 nm) is consistent with the absorption range of the films, and to the progressive drop of transmittance in the visible [31]. At 510 °C, the crystallization of Cu and Fe_3O_4 phases having lower refractive indices than Cu_2O and Fe_2O_3 phases would be one reason of the decrease of the refractive index in infrared range. For lower wavelengths (< 1000 nm), the "OJL" dispersion model taking into account the strong optical absorption exhibits two maxima in the refractive index which are related to the two OJL interband electronic transitions. In agreement with the absorption spectra, a slight difference of the refractive index behaviour can be observed according to the deposition temperature, which is suppposed to be related to the change in the preferential orientation. Indeed, a few studies underline the anisotropic behaviour of the optical properties in delafossite compounds [37][38]. Furthermore, electronic structure calculations on delafossite compound such as $CuAlO_2$ reported on the different optical behaviour according to the cristallographic directions [39][40]. It was shown that both refractive index and dispersion are smaller in the direction parallel to the c-axis than in its perpendicular direction. A similar behaviour, based on the computed anisotropic absorption spectra in $CuFeO_2$, would also be responsible of the slight decrease of the refractive index at 510 °C.

Optical gap energy (Fig. 6(a)) was determined using the graphical method in which the absorption coefficient calculated from the equation (2) was used in Tauc's plots considering direct interband electronic transition. In agreement with our above observations on the poor average transmittance in the visible and of the modelled dielectric functions to simulate transmittance and reflectance spectra, only two linear regions were observed indicating the presence of two direct transitions (not shown here), while 3 main transitions are computed in the visible range [3][4]. A first transition at 1.62 eV is independent on the deposition temperature, whereas the 2nd transition decreases from 2.26 to 2.10 eV as the deposition temperature increases from 380 to 510 °C. Other references experimentally showed by spectrometry and photoconductivity presence of both transitions [4][33]. The 2nd transition could be ascribed to O-p_x, -p_y $\rightarrow$ Cu-d_{z2} (O-2p $\rightarrow$ Cu-3d) and O-p_x, -p_y $\rightarrow$ Fe-d_{xy}, -d_{xz}, -d_{yz}, -d_{x2-y2}, -d_{z2} (O-2p $\rightarrow$ Fe-3d) at 1.92 eV [4]. Furthermore, it is noteworthy that, with the deposition temperature elevation, the amplitude ratios of the 1st transition over the 2nd

transition determined from "OJL" model increase (x 3.5 at 380 °C to x 9.5 at 510 °C). This means that the 1st transition prevails over the 2nd one while both amplitudes increases with temperature. The 1st transition at 1.4 - 1.62 eV involves transition along the c direction (O-$2p_z$ -> Fe-$3d_{z2}$ at 1.55 eV) [4]. The prevailing of the 1st transition is then consistent with the observed change of the preferential orientation along the [006] direction at elevated deposition temperature. Moreover Ong et al. [3] demonstrated that the optical bandgap energies at 1.8 and 2.15 eV are well ascribed to absorption components parallel and perpendicular to the c-axis direction, respectively. Accordingly, the slight difference in the observed absorption spectra below 500 nm could then be related to the observed change in the preferential orientation. However it should be mentionned that in highly oriented thin films along the c axis, containing small amount of cuprospinel phase, the transition at 2.1 eV is still observed meaning that many transition modes are implied simultaneously [33].

In the crystalline solids, material disorder stems from local composition (doping, substitution), structure (vacancy, dislocation, deviation from stoichiometry) or temperature changings (lattice thermal vibrations), and manifests through the presence of localized states near the band edges forming absorption tail at energies below E_g [41]. Only structural disordering is presuming to have a significant effect in our case, because of the constancy of the chemical composition in sputtered films and because measurements have been done at ambient temperature. While the origin of the tail state remains unclear, their distribution shows an exponential dependence with the energy below the bandgap [32]. In the "OJL" interband electronic transition, the parameter γ describes the width of the tail states exponentially decaying into the bandgap (Fig. 6(b)). Besides, the well-known Urbach tail, expressing the width of the exponential tail in the absorption spectrum for energies below the bandgap has been also computed using the equation:

$$\alpha(h\nu)=\alpha_0 \exp\left(\frac{h\nu-E_0}{E_u}\right) \qquad (9)$$

where α is the absorption coefficient (cm^{-1}), h the Planck's constant, ν the frequency of the incident electromagnetic wave (Hz), α_0 and E_0 are characteristic parameters related to the materials corresponding to the convergence point of the Urbach bundle (extrapolation of lines ln(α) vs. energy for different temperatures) [41][43]. E_u is the Urbach energy (eV) and expresses the width of the band associated to the disorder. Both methods result in the same order of magnitude and the

same trend, namely a progressive decrease of the band width related to the disorder when increasing the deposition temperature. Despite the relatively large values for the film deposited at 380 °C, the γ and E_u parameters are consistent with values reported previously for delafossite $CuFeO_2$ thin films (~ 130 nm) [16], and also for sputtered crystallized oxides such as undoped NiO [42], or undoped ZnO [43]. It has to be specified that, in reason of the 1st transition located below the energy of the 2nd transition, the determination of the Urbach energy cannot be obtained. Estimated by modelling, the 2nd transition displays a very large γ energy (~ 0.3-0.45 eV). The relaxation of the intrinsic stress which develops during the film growth is probably responsible of the decrease of the disorder with the elevation of the deposition temperature rather than thermal tensile stress which appears due to the difference of thermal expansion coefficient between the substrate ($0.5\ 10^{-6}\ K^{-1}$) and the film ($2.61\ 10^{-6}\ K^{-1}$ [44]) during the cooling step. The growth of crystallite size combined with the dislocation density supports this observation.

3.3 Electronic transport properties

The temperature dependence of the electrical conductivity along with the charge carrier concentration vs. mobility is depicted in Fig. 7(a) and (b). The film deposited at 510 °C is too resistive to be characterized by our Hall effect setup. To confirm its poor electrical conductivity, the 4 probes method has been implemented on the samples (Table 1). Both methods (4 probes method or Hall effect) indicate that the electrical conductivity of the films deposited between 380 and 460 °C has the same order of magnitude. According to Mayadas and Shatzkes model [45], the electrical conductivity is driven by the charges scattering at the grain boundaries. This effect becomes more significant with the grain size reduction in metallic environment (< 30 nm in Al) [46]. The mean free path of charge carrier in $CuFeO_2$, calculated from the charge carrier concentration and mobility, being less than 1 nm and about 350 times lower than that of a Cu single-crystal (~ 39 nm) [46] cannot ascertain the dependency of the electrical conductivity on the grain boundary for the films deposited at temperatures lower than 510 °C.

As expecting for a semi-conductor, the electrical conductivity well increases with the temperature, due to the increase of carrier concentration with the temperature elevation (Fig. 7(a)). The Seebeck coefficient, representing the thermoelectric response induced by a temperature difference, was also

measured (Table 1). The Seebeck coefficient is related to the charge carrier diffusion towards the cold side due to a temperature gradient. Then, according to the sign convention, a positive coefficient means that the electrical conductivity is dominated by positive charge carriers. The previously established hypothesis that oxygen deficiencies, which lead to the formation of donor levels [5], would be created by increasing the substrate temperature is then not verified. Based on Cu_2O chemistry, it could be assumed that the defects responsible of the p-type behaviour would be rather related to copper vacancies, the delafossite having weak tolerance for Cu non-stoichiometry, and/or interstitial oxygen defects while having higher activation energy and thus a lower probability to occur [1][47]. However, a study dealing with the cationic vacancy in $CuGaO_2$ revealed that the p-type charge carrier is rather related to oxygen overstoichiometry [48]. Furthermore, the linearity of the plots $\ln(\sigma)$ vs. $T^{-1/4}$ implies that a mechanism of hopping occurs [5][49].

The temperature dependence of the electrical conductivity is almost not more perceptible at 550 °C due to the presence of metallic and semi-metallic phases, and also confirmed by the weak evolution of the charge carrier concentration with the temperature. The crystallization of highly electrical conductive phases such as Cu or semimetal Fe_3O_4 having an electrical conductivity of about $3\ 10^6$ and 10^4 S m^{-1}, respectively [31][50], is responsible of the observed increase in the electrical conductivity. Likewise, the formation in weak proportion of Fe_2O_3 and Cu_2O phases (Cu_2O 10^{-2} S m^{-1}, Fe_2O_3 10^{-8} to 10^{-2} S m^{-1}) in agreement with the absorption coefficient and refractive index observations in the infrared would explain the rather low electrical conductivity for film deposited at 460 °C.

Previous articles have reported that the electrical conductivity via the charge carrier mobility exhibits a relatively strong anisotropy along or perpendicular to the c direction, and that the charge carrier mobility strongly depends on the nature of the majority charge carrier [2][5]. Indeed, Benko et al. [2] demonstrated that the mobility of charge carrier in p-type $CuFeO_2$ ($\sim 10^{-5}$ $m^2V^{-1}s^{-1}$) is higher than n-type compounds ($\sim 10^{-10}$ $m^2V^{-1}s^{-1}$). Furthermore, Shannon et al. [51] observed an anisotropic electrical conductivity according to the crystallographic orientations. Indeed, the electrical conductivity ratio $\sigma_{//}/\sigma_{\perp}$ or mobility ratio $\mu_{//}/\mu_{\perp}$ (// parallel to c axis), estimated from Dordor et al. [5] data, is around $2.1\ 10^{-3}$ for n-type whereas it tends to $2.6\ 10^{-1}$ in p-type compound, showing the promotion of the electrical conductivity along the (a,b) plane, i.e. parallel to the Cu^+

layers. The order of magnitude of the charge carrier mobility in the $CuFeO_2$ films deposited from 380 to 460 °C and their electrical conductivity of about few S m^{-1} ascertains the positive nature of the majority charge carrier. According to the above statements, the change in the preferential orientation towards the [006] direction because of the strong anisotropic behaviour of the electrical conductivity of the delafossite structure could then be partially responsible of the decrease of the electrical conductivity for films deposited at $T_S \geq 460$ °C (Fig. 7(a)). In our case, the electrical conductivity ratio $\sigma_{510\ °C}/\sigma_{440\ °C}$ is around 10^{-3} which is lower than the expected electrical conductivity ratio ($\sigma_{510\ °C}/\sigma_{440\ °C} \approx 0.26$), meaning that the electrical conductivity for film having a [006] preferential orientation is lower than expected (~ 2 10^{-1} S m^{-1}). Again, the presence of secondary phases in a weak proportion, such as Fe_2O_3 or Cu_2O phases would contribute to the low electrical conductivity as observed by the 4 probe methods.

3.4 Magnetic properties

Magnetization loops measured at room temperature for delafossite films deposited at different deposition temperatures are displayed in Fig. 8(a). The quasi-linear dependency of the magnetization on the applied magnetic field in addition with the absence of saturation magnetization suggests that paramagnetic behaviour dominates as expected at this temperature, largely higher than the Néel transition temperatures for the delafossite compound [52][53]. Assuming a pure paramagnetic behaviour, the mean volume susceptibility (i.e. the ratio between the variation of the magnetization and the applied magnetic field) has been calculated for a magnetic field greater than 0.5 T (Table 1). Up to 510 °C, these mean volume susceptibilities are about 2.5 x 10^{-2}, which is between 2 and 9 times higher than the previously reported values at room temperature for single crystal [54][55]. It is noteworthy that these values are anisotropic only in the antiferromagnetic state [54]. The variations in the mean volume susceptibility reveal local fluctuation in the chemical composition (e.g. Cu vacancy, O insertion, etc) of the paramagnetic $CuFeO_2$ phase [56].

In fact, each magnetization loop in Fig. 8(a) exhibits a low coercive field and a low residual magnetization combined with a change in the slope of the magnetization at low applied magnetic field. It is noteworthy that the magnetization loops are similar to that of canted antiferromagnetic

materials [56]. However, this phenomenon probably not occur due to the large temperature difference between Néel's temperature and room temperature [57][58] and also to the presence of secondary phases as deduced from the optical and electrical studies. This shows that in addition to the overall paramagnetic behaviour, a small fraction of short-range ferromagnetic phase is present. This phase could be attributed to the chemical ordering at the nanoscale or to ferromagnetic clusters, as suggested by the crystallization of magnetite at the highest deposition temperature. Subtracting the paramagnetic component to the measured magnetization, the saturation magnetization related to the ferromagnetic component has been estimated in Fig. 8(b). These values are rather stable at 10 kA m^{-1} up to 460 °C. Afterwards the saturation magnetization progressively increases with the deposition temperature, confirming the increase of the ferromagnetic component with the deposition temperature. The saturation magnetization is too high to correspond to pure hematite Fe_2O_3 (M_s ~ 1-2 kA m^{-1}). The crystallisation of the cuprospinel $CuFe_2O_4$ seems improbable considering the rather reductive conditions with the deposition temperature increase. Assuming the crystallization of magnetite cluster (or eventually of γ-Fe_2O_3) which exhibits a theoretical saturation magnetization of about 477 (350) kA m^{-1} [59] could be responsible for such ferromagnetic behaviour, the volume fraction of this ferromagnetic phase would only be 2 (3) % for the films deposited below 460 °C, 3 (5) % for film deposited at 510 °C and up to 10 % for film grown at 550 °C finally showing X-ray detectable magnetite phase.

4. Conclusions

Delafossite $CuFeO_2$ films have been synthesized by reactive magnetron sputtering on heated fused silica substrate. $CuFeO_2$ films crystallize in the rhombohedral structure from 380 to 550 °C, with a preferential orientation change from [012] to [006] direction between 460 and 510 °C. It is shown that the increase of deposition temperature makes the deposition conditions more reductive, leading to the formation of secondary phases with decreasing oxidation state, detected from optical and electrical studies. Beyond 510 °C, the partial reduction of the delafossite in Cu and Fe_3O_4 phases occurs. By optical modelling, two absorption peaks were assigned to the light absorption in the parallel and perpendicular directions to the c-axis. The electrical conductivity, dominated by positive charge carrier, exhibits a relatively strong dependency on the crystallographic orientation. In addition to the paramagnetic behaviour, a short-range ferromagnetic component is shown even

at low deposition temperature (380 °C), while its presence by X-ray diffraction is not detected. It is suggested that an increase of the deposition temperature at a constant oxygen partial pressure would progressively dissociate the delafossite phase in addition to change its preferential orientation. This would occur by forming phases with decreasing oxidation state contributing to the optical and electrical behaviour by their nature and their proportion. It is believed that the decrease of the relative poor transmittance in the visible range is ascribed to the presence of such phases growing with temperature.

Acknowledgement

The authors thank the community “Pays de Montbéliard Agglomération” for his financial support and would like to express their gratitude for the financial support received from Mouloud Mammeri University of TiziOuzou, Algeria

References

[1] M. A. Marquardt, N. A. Ashmore, D. P. Cann, Crystal chemistry and electrical properties of the delafossite structure, Thin Solid Films 496 (2006) 146, https://doi.org/10.1016/j.tsf.2005.08.316

[2] F. A. Benko, F. P. Koffyberg, Opto-electronic properties of p- and n-type delafossite $CuFeO_2$, J. Phys. Chem. Solids 48 (1987) 431, https://doi.org/10.1016/0022-3697(87)90103-X

[3] K. P. Ong, K. Bai, P. Blaha, P. Wu, Electronic structure and optical properties of $AFeO_2$ (A = Ag, Cu) within GGA calculations, Chem. Mater. 19 (2007) 634, https://doi.org/10.1021/cm062481c

[4] Q.-L. Liu, Z.-Y. Zhao, R.-D. Zhao, J.-H. Yi, Fundamental properties of delafossite $CuFeO_2$ as photocatalyst for solar energy conversion, J. Alloy. Compd. 819 (2020) 153032, https://doi.org/10.1016/j.jallcom.2019.153032

[5] P. Dordor, J. P. Chaminade, A. Wichainchai, E. Marquestaut, J. P. Doumerc, M. Pouchard, P. Hagenmuller, Crystal growth and electrical properties of $CuFeO_2$ single crystals, J. Solid State Chem. 75 (1988) 105, https://doi.org/10.1016/0022-4596(88)90307-6

[6] A. P. Mackenzie, The properties of ultrapure delafossite metals, Rep. Prog. Phys., 80 (2017) 032501, https://doi.org/10.1088/1361-6633/aa50e5

[7] T. Joshi, T. R. Senty, R. Trappen, J. Zhou, S. Chen, P. Ferrari, P. Borisov, X. Song, M. B. Holcomb, A. D. Bristow, A. L. Cabrera, D. Lederman, Structural and magnetic properties of epitaxial delafossite $CuFeO_2$ thin films grown by pulsed laser deposition, J. Appl. Phys. 117 (2015) 013908, http://dx.doi.org/10.1063/1.4905424

[8] M. M. Moharam, M. M. Rashad, E. M. Elsayed, R. M. Abou-Shahba, A facile novel synthesis of delafossite $CuFeO_2$ powders, J. Mater. Sci.: Mater. Electron. 25 (2014) 1798, https://doi.org/10.1007/s10854-014-1801-x

[9] R. Daou, R. Frésard, V. Eyert, S. Hébert, A. Maignan, Unconventional aspects of electronic transport in delafossite oxides, Sci. Technol. Adv. Mat., 18 (2017) 919, https://doi.org/10.1080/14686996.2017.1393633

[10] T. Zhao, Q.-L. Liu, Z.-Y. Zhao, High-throughput screening delafossite $CuMO_2$ (M = IIIA, 3d, 4d, 5d, and RE) optoelectronic functional materials based on first-principles calculations, J. Phys. Chem. C 123 (2019) 14292, https://doi.org/10.1021/acs.jpcc.9b04481

[11] C. Rudradawong, C. Ruttanapun, Effect of excess oxygen for $CuFeO_{2.06}$ delafossite on thermoelectric and optical properties, Physica B. 526 (2017) 21, https://doi.org/10.1016/j.physb.2017.09.046

[12] M. Tato, R. Shimonishi, M. Hagiwara, S. Fujihara, Reactive templated grain growth and thermoelectric power factor enhancement of textured $CuFeO_2$ ceramics, ACS Appl. Energy Mater. 3 (2020) 1979, https://doi.org/10.1021/acsaem.9b02407

[13] H. Dong, Z. Li, X. Xu, Z. Ding, L. Wu, X. Wang, X. Fu, Visible light-induced photocatalytic activity of delafossite $AgMO_2$ (M = Al, Ga, In) prepared via a hydrothermal method, Appl. Catal. B-Environ. 89 (2009) 551, https://doi.org/10.1016/j.apcatb.2009.01.018

[14] Q. Xu, R. Li, C. Wang, D. Yuan, Visible-light photocatalytic reduction of Cr(VI) using nano-sized delafossite ($CuFeO_2$) synthesized by hydrothermal method, J. Alloy. Compd. 723 (2017) 441, https://doi.org/10.1016/j.jallcom.2017.06.243

[15] S. Z. Li, J. Liu, X. Z. Wang, B. W. Yan, H. Li, et J.–M. Liu, Epitaxial growth of delafossite $CuFeO_2$ thin films by pulsed laser deposition, Phys. B Condens. Matter. 407 (2012) 2412, https://doi.org/10.1016/j.physb.2012.03.037

[16] A. H. Omran Alkhayatt, S. M. Thahab, I. A. Zgair, Structure, surface morphology and optical properties of post-annealed delafossite $CuFeO_2$ thin films, Optik, 127 (2016) 3745, https://doi.org/10.1016/j.ijleo.2015.12.144

[17] H. Mohamed, E. Chikoidze, A. Ratep, A. M. A. Elsoud, M. Boshta, M. B. S. Osman, Synthesis of conducting single-phase $CuFeO_2$ thin films by spray pyrolysis technique, Mat. Sci. Semicon. Proc., 107 (2020) 104831, https://doi.org/10.1016/j.mssp.2019.104831

[18] H.-Y. Chen, J.-H. Wu, Characterization and optoelectronic properties of sol–gel-derived $CuFeO_2$ thin films, Thin Solid Films 520 (2012) 5029, https://doi.org/10.1016/j.tsf.2012.03.032

[19] H.-Y. Chen, G.-W. Fu, Influences of post-annealing conditions on the formation of delafossite–$CuFeO_2$ thin films, Appl. Surf. Sci. 288 (2014) 258, https://doi.org/10.1016/j.apsusc.2013.10.017

[20] I. Sinnarasa, Y. Thimont, A. Barnabé, M. Beaudhuin, A. Moll, J. Schorne-Pinto, P. Tailhades, L. Presmanes, Microstructural and transport properties of Mg doped $CuFeO_2$ thin films: A promising material for high accuracy miniaturized temperature sensors based on the Seebeck effect, J. Alloys Compd. 827 (2020) 154199, https://doi.org/10.1016/j.jallcom.2020.154199

[21] Z. Deng, X. Fang, X. Wang, S. Wu, W. Dong, J. Shao, R. Tao, Characterization of amorphous p-type transparent $CuFeO_2$ thin films prepared by radio frequency magnetron sputtering method at room temperature, Thin Solid Films 589 (2015) 17, https://doi.org/10.1016/j.tsf.2015.04.066

[22] A. Barnabé, E. Mugnier, L. Presmanes, P. Tailhades, Preparation of delafossite $CuFeO_2$ thin films by rf-sputtering on conventional glass substrate, Mater. Lett., 60 (2006) 3468, https://doi.org/10.1016/j.matlet.2006.03.033

[23] Z. Deng, X. Fang, S. Wu, S. Wang, W. Dong, J. Shao, R. Tao, The effect of oxygen partial pressure on the properties of $CuFeO_2$ thin films prepared by RF sputtering, Vacuum 115 (2015) 1, https://doi.org/10.1016/j.vacuum.2015.01.025

[24] Y. Li, L. Chen, Q. Deng, Y. Shen, G. Wang, S. Wang, Effect of lack of oxygen on optical and electrical properties of RF magnetron sputtering deposited $CuFeO_{2-x}$ thin films, Mod. Phys. Lett. B, 32 (2018) 1850379, https://doi.org/10.1142/S0217984918503797

[25] I. Jouanny, A. Billard, T. Huu Loi, V. Demange, E. Bauer-Grosse, Sputtered $Fe_{1-x}(N_{1-y}C_y)_x$ films obtained in various (Ar-N_2-CH_4) reactive plasmas, Surf. Coat. Technol. 200 (2005) 1690, https://doi.org/10.1016/j.surfcoat.2005.08.075

[26] http://www.mtheiss.com/

[27] A. Zhou, W. Wang, X. Yao, B. Yang, J. Li, Q. Zhao, C. Wang, D. Xu, P. Ziolkowski, E. Mueller, Impact of the film thickness and substrate on the thermopower measurement of

thermoelectric films by the potential-Seebeck microprobe (PSM), Appl. Therm. Eng. 107 (2016) 552, https://doi:10.1016/j.applthermaleng.2016.05.037

[28] G. K. Williamson, R. E. Smallman, III. Dislocation densities in some annealed and cold-worked metals from measurements on the X-ray debye-scherrer spectrum, The Philosophical Magazine: A Journal of Theoretical Experimental and Applied Physics, 1 (1956) 34, https://doi:10.1080/14786435608238074

[29] A. Barnabé, A. Chapelle, L. Presmanes, P. Tailhades, Copper and iron based thin film nanocomposites prepared by radio frequency sputtering. Part I: elaboration and characterization of metal/oxide thin film nanocomposites using controlled in situ reduction process, J. Mater. Sci. 48 (2013) 3386, https://doi.org/10.1007/s10853-012-7123-6

[30] C.-M. Jiang, S. E. Reyes-Lillo, Y. Liang, Y.-S. Liu, G. Liu, F. M. Toma, D. Prendergast, I. D. Sharp, J. K. Cooper, Electronic structure and performance bottlenecks of $CuFeO_2$ photocathodes, Chem. Mater. 31 (2019) 2524, https://doi.org/10.1021/acs.chemmater.9b00009

[31] E. Aubry, T. Liu, A. Dekens, F. Perry, S. Mangin, T. Hauet, A. Billard, Synthesis of iron oxide films by reactive magnetron sputtering assisted by plasma emission monitoring, Mat. Chem. Phys. 223 (2019) 360, https://doi.org/10.1016/j.matchemphys.2018.11.010

[32] S. K. O'Leary, S. R. Johnson, P. K. Lim, The relationship between the distribution of electronic states and the optical absorption spectrum of an amorphous semiconductor: An empirical analysis, J. Appl. Phys. 82 (1997) 3334, https://doi.org/10.1063/1.365643

[33] Role of $CuAlO_2$ as an absorber layer for solar energy converter epitaxial thin film by photoconductivity, SN Appl. Sci. 1 (2019) 1322, https://doi.org/10.1007/s42452-019-1387-2

[34] M. Fox, Optical properties of solids, 2001, Oxford University Press

[35] H. Ben Jbara, E. Aubry, M. Kanzari, A. Billard, M. Arab Pour Yazdi, Effect of thermal annealing on the optoelectronic properties of Cu-Fe-O thin films deposited by reactive

magnetron co-sputtering, Thin Solid Films 721 (2021) 138538, https://doi.org/10.1016/j.tsf.2021.138538

[36] M. N. Polyanskiy, "Refractive index database," https://refractiveindex.info

[37] J. Pellicer-Porres, A. Segura, D. Kim, Refractive index of the $CuAlO_2$ delafossite, Semicond. Sci. Tech. 24 (2008) 015002, https://doi.org/10.1088/0268-1242/24/1/015002

[38] C. C. Homes, S. Khim, A. P. Mackenzie, Perfect separation of intraband and interband excitations in $PdCoO_2$, Phys. Rev. B 99 (2019) 195127, https://doi.org/10.1103/PhysRevB.99.195127

[39] N. N. Som, V. Sharma, V. Mankad, M.L.C. Attygalle, P. K. Jha, Role of $CuAlO_2$ as an absorber layer for solar energy converter, Sol. Energy 193 (2019) 799, https://doi.org/10.1016/j.solener.2019.09.098

[40] K. C. Bhamu, R. Khenata, Saleem Ayaz Khan, Mangej Singh, K. R. Priolkar, Electronic, optical and thermoelectric properties of 2H-$CuAlO_2$: A first principles study, J. Electron. Mater. 45 (2016) 615, https://doi.org/10.1007/s11664-015-4160-3

[41] I. Studenyak, M. Kranjec, M. Kurik, Urbach rule in solid state physics, International Journal of Optics and Applications, 4 (2014) 76, https://doi:10.5923/j.optics.20140403.02

[42] M.S. Jamal, S.A. Shahahmadi, P. Chelvanathan, H. F. Alharbi, M. R. Karim, M. Ahmad Dar, M. Luqman, N. H. Alharthi, Y. S. Al-Harthi, M. Aminuzzaman, N. Asim, K. Sopian, S.K. Tiong, N. Amin, Md. Akhtaruzzaman, Effects of growth temperature on the photovoltaic properties of RF sputtered undoped NiO thin films, Results Phys. 14 (2019) 102360, https://doi.org/10.1016/j.rinp.2019.102360

[43] R. C. Rai, Analysis of the Urbach tails in absorption spectra of undoped ZnO thin films, J. Appl. Phys. 113 (2013) 153508, http://dx.doi.org/10.1063/1.4801900

[44] N. P. Salke, K. Kamali, T.R. Ravindran, G. Balakrishnan, R. Rao, Raman spectroscopic studies of $CuFeO_2$ at high pressures, Vib. Spectrosc. 81 (2015) 112, https://doi.org/10.1016/j.vibspec.2015.10.010

[45] A. F. Mayadas, M. Shatzkes, Electrical-resistivity model for polycrystalline films: The case of arbitrary reflection at external surfaces, Phys. Rev. B 1 (1970) 1382, https://doi.org/10.1103/PhysRevB.1.1382

[46] J. M. E. Harper, C. Cabral Jr., P. C. Andricacos, L. Gignac, I. C. Noyan, K. P. Rodbell, C. K. Hu, Mechanisms for microstructure evolution in electroplated copper thin films near room temperature, J. Appl. Phys. 86 (1999) 2516, https://doi.org/10.1063/1.371086

[47] H. Yanagi, S. Inoue, K. Ueda, H. Kawazoe, H. Hosono, N. Hamada, Electronic structure and optoelectronic properties of transparent p-type conducting $CuAlO_2$, J. Appl. Phys. 88 (2000) 4159, https://doi.org/10.1063/1.1308103

[48] N. A. Ashmore, D. P. Cann, Electrical and structural characteristics of non-stoichiometric Cu-based delafossites, J. Mater. Sci. 40 (2005) 3891, https://doi.org/10.1007/s10853-005-0781-x

[49] F.-C. Chiu, A review on conduction mechanisms in dielectric films, Adv. Mater. Sci. Eng. 2014 (2014) 578168, https://doi.org/10.1155/2014/578168

[50] P. N. Hishimone, H. Nagai, M. Morita, T. Sakamoto, M. Sato, Highly-conductive and well-adhered Cu thin film fabricated on quartz glass by heat treatment of a precursor film obtained via spray-coating of an aqueous solution involving Cu(II) complexes, Coatings 8 (2018) 352, https://doi.org/10.3390/coatings8100352

[51] R. D. Shannon, D. B. Rogers, C. T. Prewitt, Joseph L. Gillson, Chemistry of noble metal oxides. III. Electrical transport properties and crystal chemistry of ABO_2 compounds with the delafossite structure, Inorg. Chem. 10 (1971) 723, https://doi.org/10.1021/ic50098a013

[52] M. M. Moharam, M. M. Rashad, E. M. Elsayed, R. M. Abou-Shahba, A facile novel synthesis of delafossite $CuFeO_2$ powders, J. Mater. Sci.: Mater. Electron. 25 (2014) 1798, https://doi.org/10.1007/s10854-014-1801-x

[53] O. A. Petrenko, M. R. Lees, G. Balakrishnan, S. de Brion, G. Chouteau, Revised magnetic properties of $CuFeO_2$—a case of mistaken identity, J. Phys.: Condens. Matter. 17 (2005) 2741, https://doi.org/10.1088/0953-8984/17/17/023

[54] Z. Hua-Kun, S. Li-Ran, X. Zheng-Cai, H. Jun-Wei, C. Bo-Rong, J. Zhao, W. Meng, O. Zhong-Wen, C. Gang, The magnetic anisotropy and complete phase diagram of $CuFeO_2$ measured in a pulsed high magnetic field up to 75 T, Chin. Phys. Lett. 32 (2015) 047502, https://doi.org/10.1088/0256-307X/32/4/047502

[55] M. John, S. Heuss-Aßbichler, S.-H. Park, A. Ullrich, G. Benka, N. Petersen, D. Rettenwander, S. R. Horn, Low-temperature synthesis of $CuFeO_2$ (delafossite) at 70 °C : A new process solely by precipitation and ageing, J. Solid State Chem. 233 (2016) 390, http://dx.doi.org/10.1016/j.jssc.2015.11.011

[56] B. D. Cullity, C. D. Graham, Introduction to magnetic materials, 2nd, IEEE press, Wiley, 2008, https://doi.org/10.1002/9780470386323

[57] K. K. Shukla, R. Singh, A. Kumar, A. K. Ghosh, S. Chatterjee, Griffith-like phase in Crednerite $CuMnO_2$, Mater. Res. Bull. 91 (2017) 135, https://doi.org/10.1016/j.materresbull.2017.03.054

[58] A. Rathi, P. K. Rout, S. Perween, R. P. Singh, P. D. Babu, A. Gupta, R. P. Pant, G. A. Basheed, Signature of a Griffiths phase in layered canted antiferromagnet Sr_2IrO_4, J. Magn. Magn. Mater. 468 (2018) 230, https://doi.org/10.1016/j.jmmm.2018.07.091

[59] M. Langlet, M. Labeau, B. Bochu, J.-C. Joubert, Preparation of thin films in the system γFe_2O_3-Fe_3O_4 for recording media by spray pyrolysis of organometallic solutions using an ultrasonic pump, IEEE T. Magn. 22 (1986) 151, http://doi.org/10.1109/TMAG.1986.1064302

Figures caption

Fig. 1 X-ray diffractograms of $CuFeO_2$ films deposited at different temperatures.

Fig. 2 Evolution of the crystallite size with the deposition temperature for 3 different crystallographic directions (// [006], [101] and [012]).

Fig. 3 Transmittance and reflectance spectra of delafossite $CuFeO_2$ films deposited at different temperatures (solid and dashed lines, respectively). Open circles and diamonds correspond to the simulated spectra with the model based on two OJL interband transitions combined with Drude-like dispersion, respectively.

Fig. 4 Absorption coefficient spectra determined with different methods (solid line: 2 OJL interband transitions with Drude-like dispersion model, dotted line: Cauchy model, dashed line: from transmittance and reflectance spectra).

Fig. 5 Refractive index vs. wavelength of delafossite thin films measured using two different models (solid line: 2 OJL interband transitions with Drude-like dispersion model and dotted line: Cauchy model).

Fig. 6 (a) Optical band gap energy vs. deposition temperature determined using two different methods: (i) modelling of the dielectric function (2 OJL interband transitions with Drude-like model), and (ii) graphical method by using Tauc's plot for direct transitions. (b) Evolution of γ broadening spread of band tails in OJL interband transition model and of Urbach energy of the transition at 1.62 eV vs. deposition temperature (Urbach energy of the 2^{nd} transition (2.26-2.10 eV) cannot be obtained in reason of the presence of the 1^{st} transition at lower energies).

Fig. 7 (a) Evolution of $\ln(\sigma)$ vs. $T^{-1/4}$ and (b) of charge carrier mobility vs. concentration for the $CuFeO_2$ films deposited at different temperatures.

Fig. 8 (a) M-H loops and (b) evolution of the coercive field and of the magnetization at saturation once subtracting the paramagnetic component for $CuFeO_2$ films deposited at various deposition temperatures.

Highlights

Rhombohedral $CuFeO_2$ films have been reactively sputtered from 380 to 550 °C

At 510 °C, the [006] preferred orientation prevails on the [012] direction

Crystal anisotropy alters the optical and electrical properties of thin films

Partial dissociation of $CuFeO_2$ occurs with the rise of deposition temperature

Table caption

Table 1 Average transmittance in visible range, electrical conductivity measured at room temperature using the 4 probes method, Seebeck coefficient and mean volume susceptibility determined from M-H loops of the $CuFeO_2$ films sputtered at different temperatures

Deposition temperature (°C)	**Average transmittance in visible range**	**Electrical conductivity at 20 °C (S m^{-1})**	**Seebeck coefficient (µV K^{-1})**	**Mean volume susceptibility**
380	0.056	$0.8\ 10^{0}$	295	$2.5\ 10^{-2}$
440	0.035	$1.3\ 10^{0}$	101	$2.1\ 10^{-2}$
460	0.025	$3.2\ 10^{0}$	196	$2.1\ 10^{-2}$
510	0.020	$3.4\ 10^{-3}$	101	$2.4\ 10^{-2}$
550	0.001	$1.3\ 10^{2}$	194	$1.4\ 10^{-2}$

Figure 1

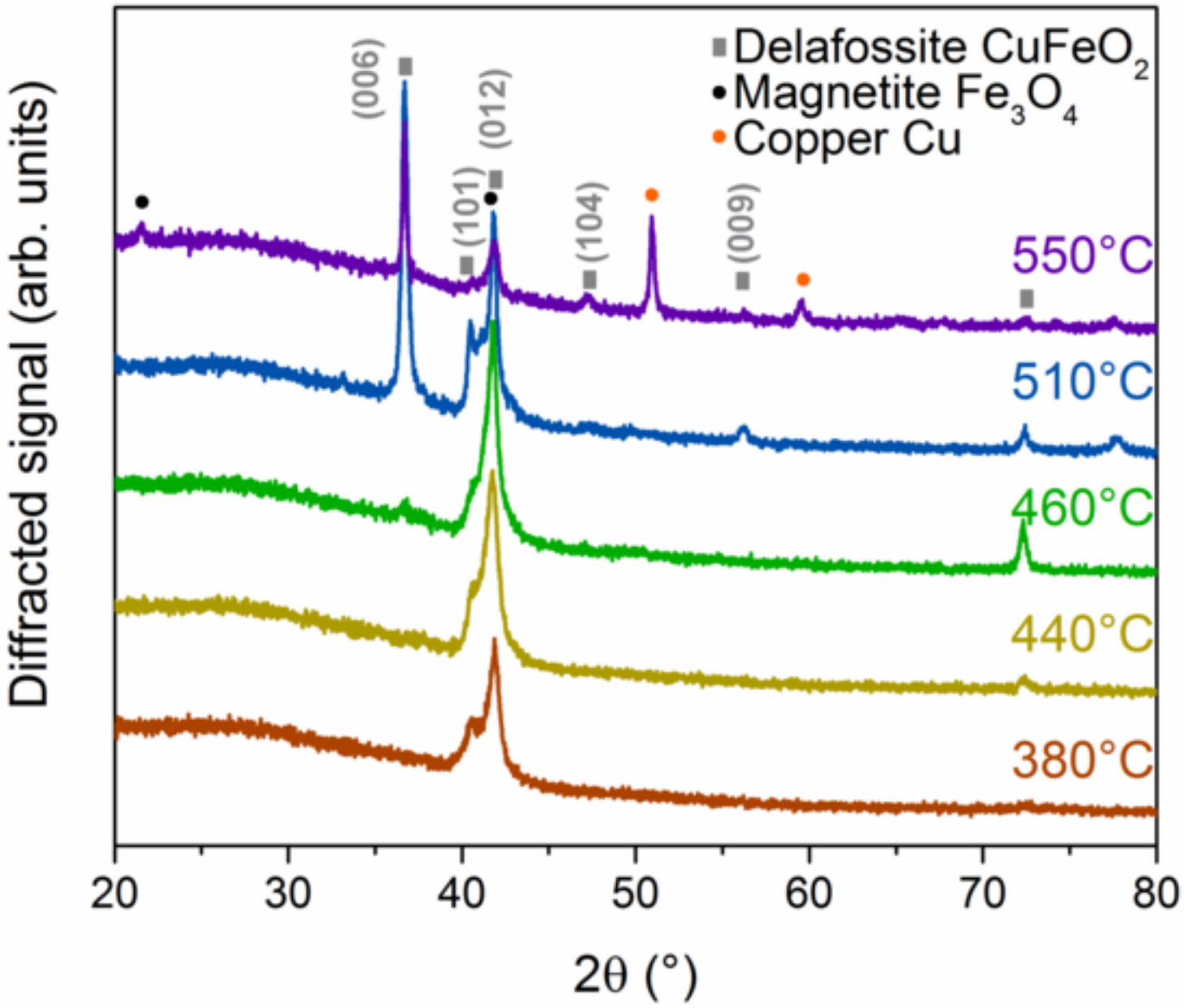

Figure 2

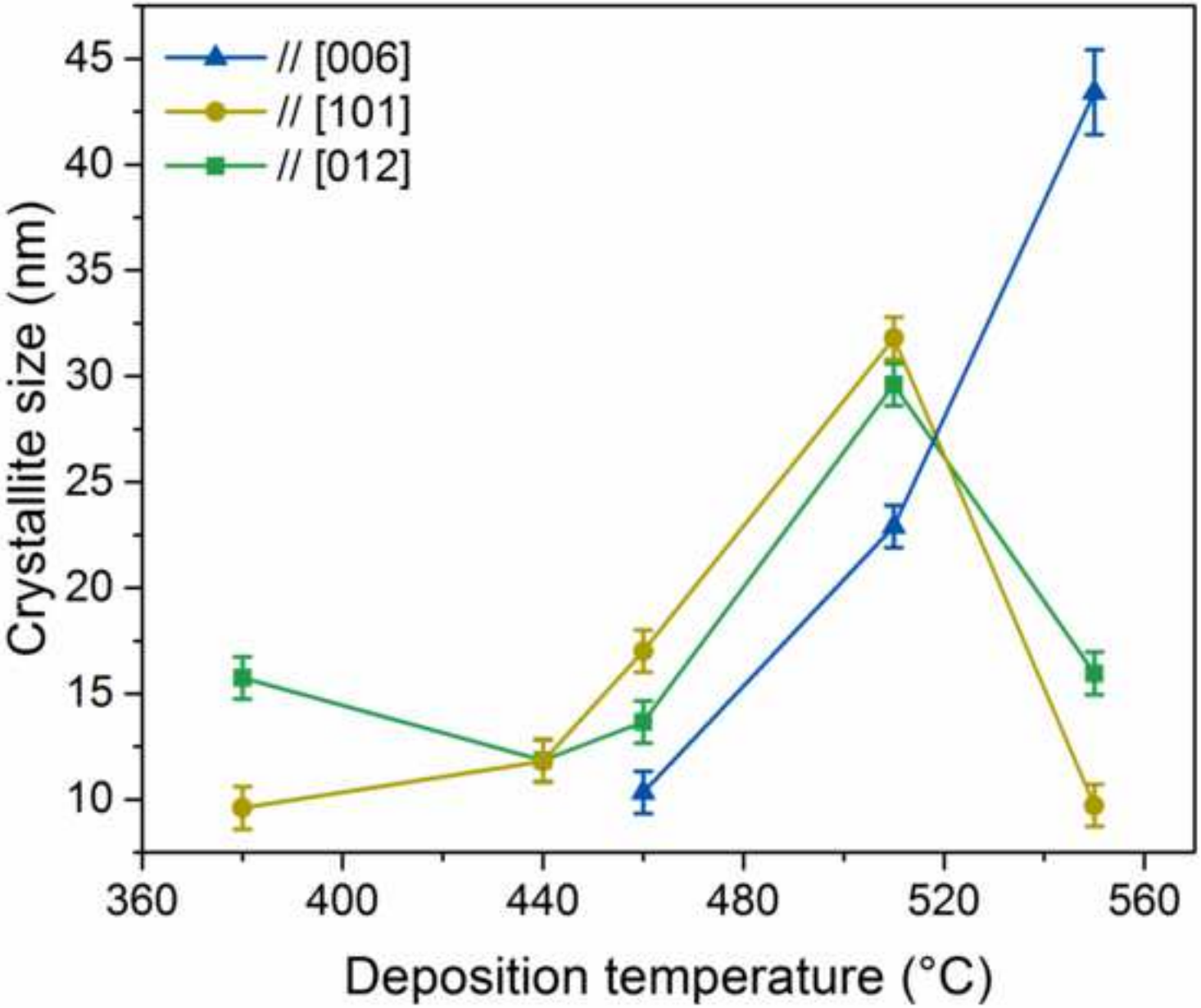

Figure 3a

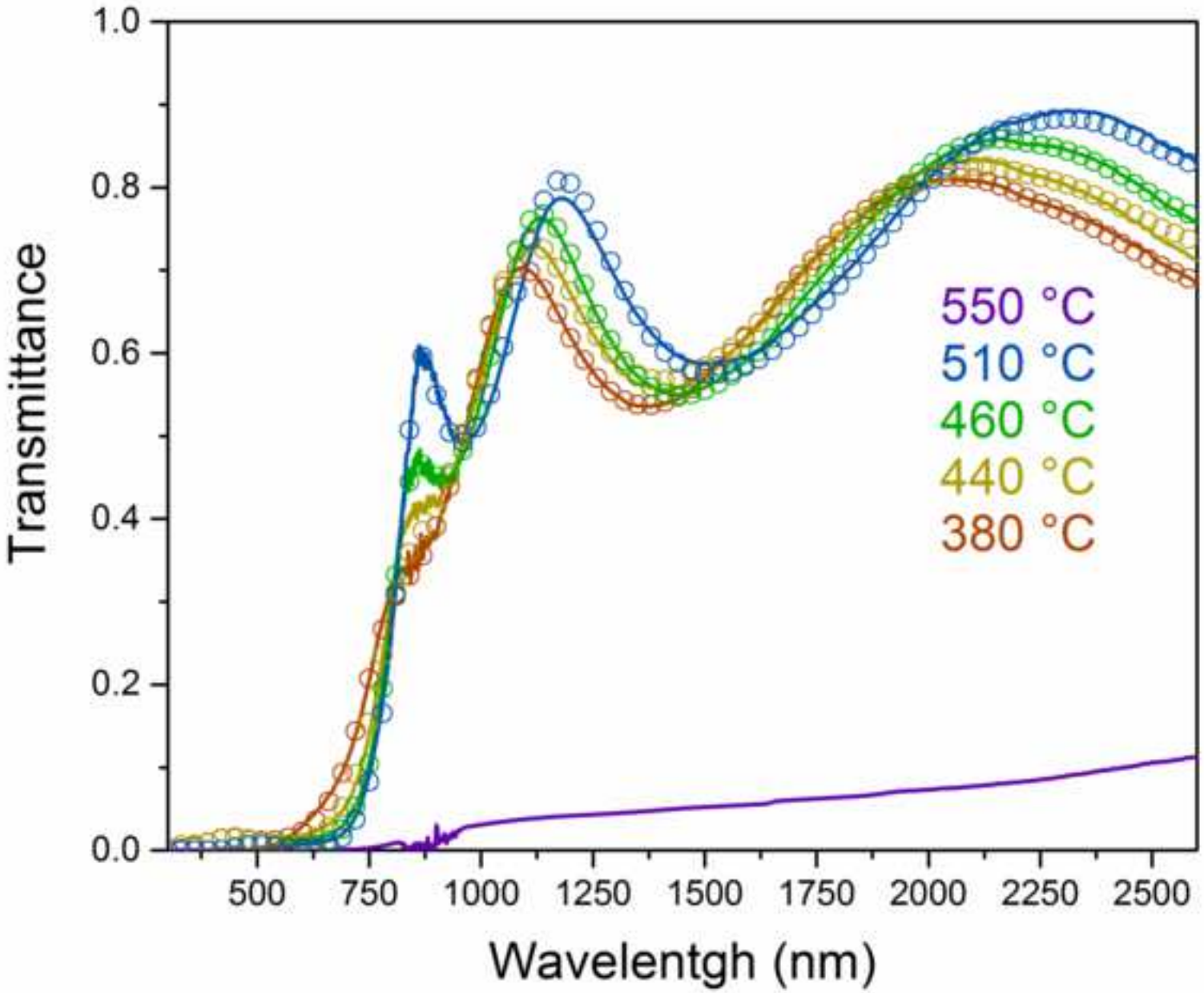

Figure 3b

Click here to access/download;Figure;Fig3b Reflectance.tif

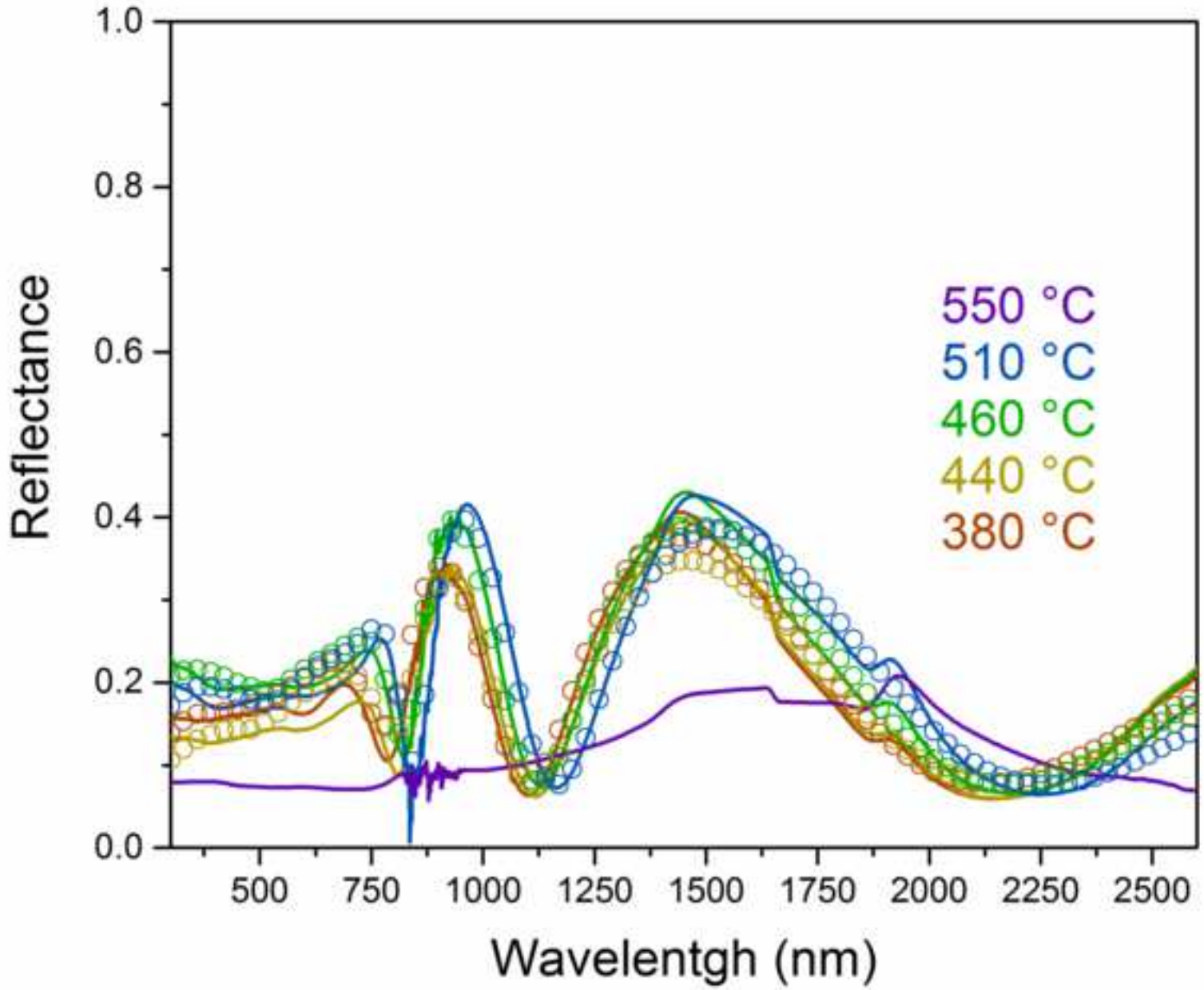

Figure 4

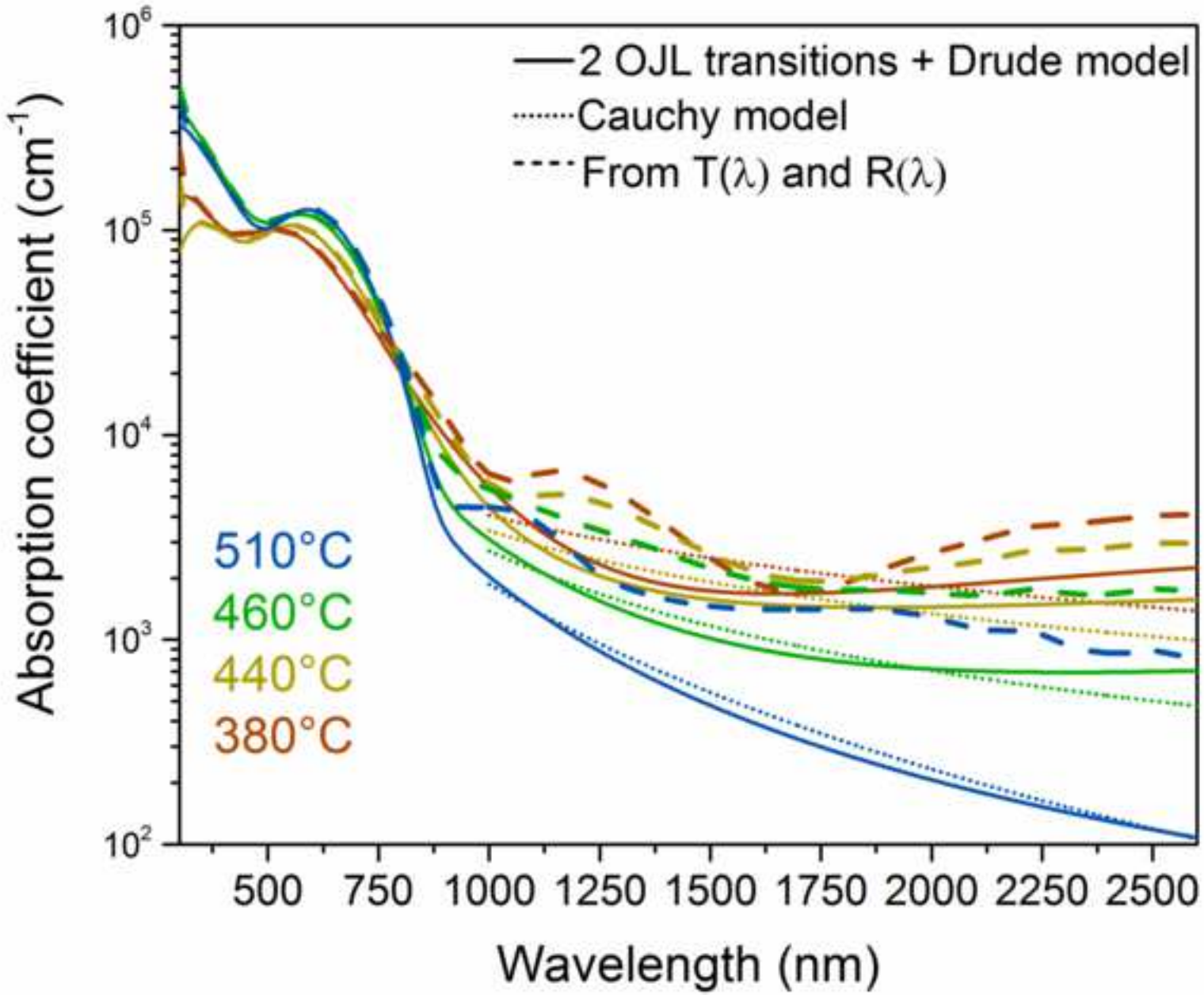

Figure 5

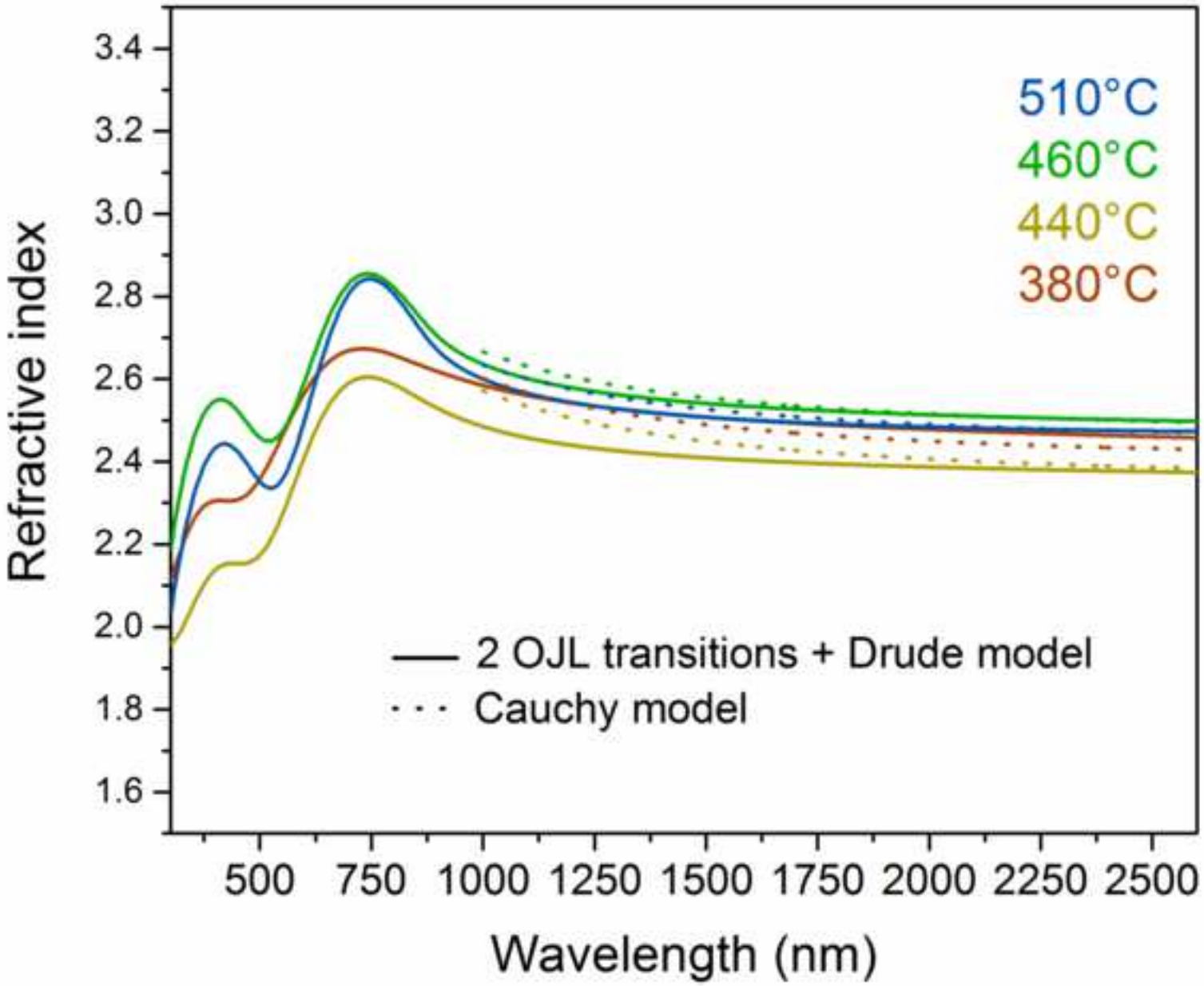

Figure 6a

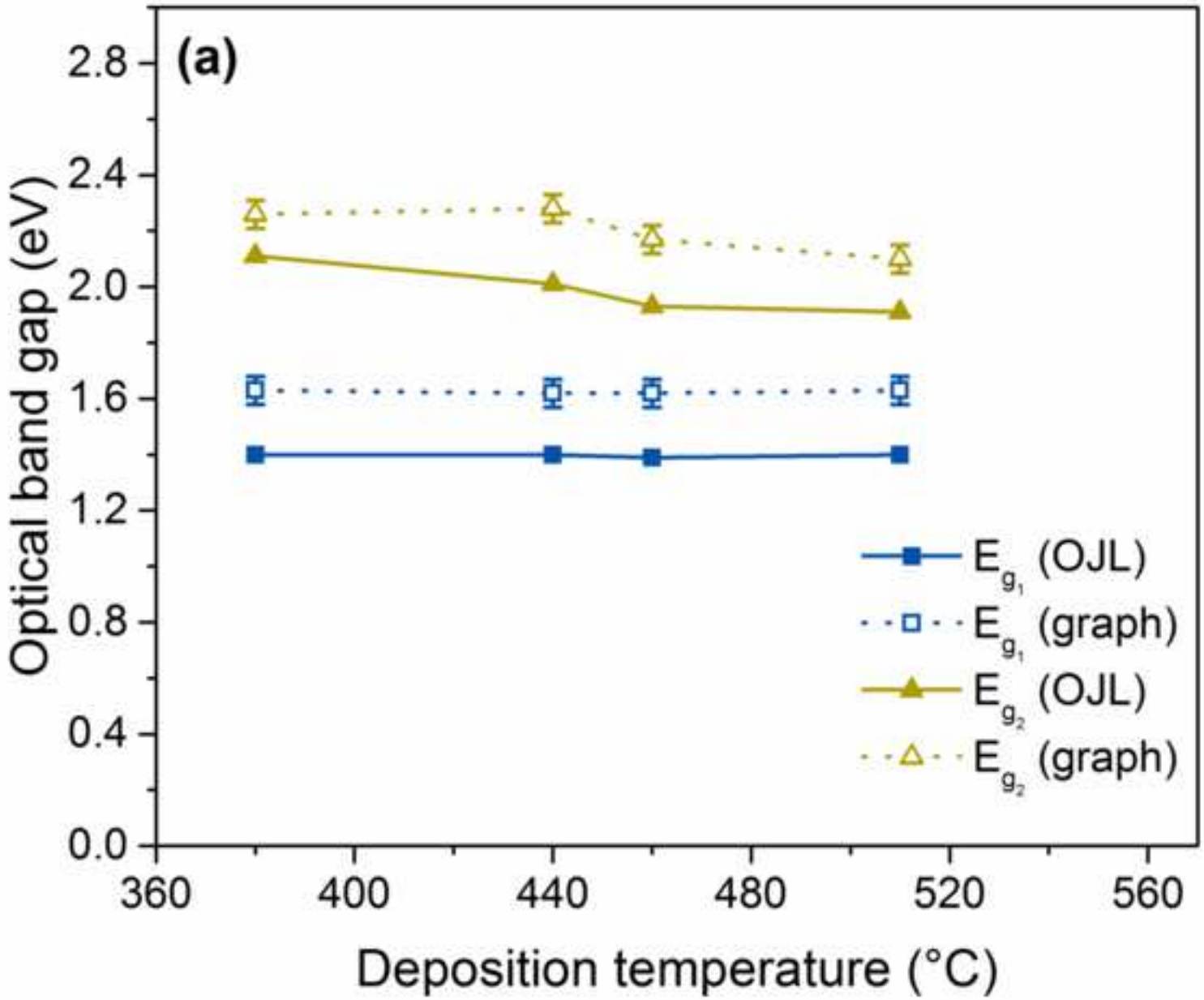

Figure 6b

Click here to access/download;Figure;Fig6b Urbach b.tif

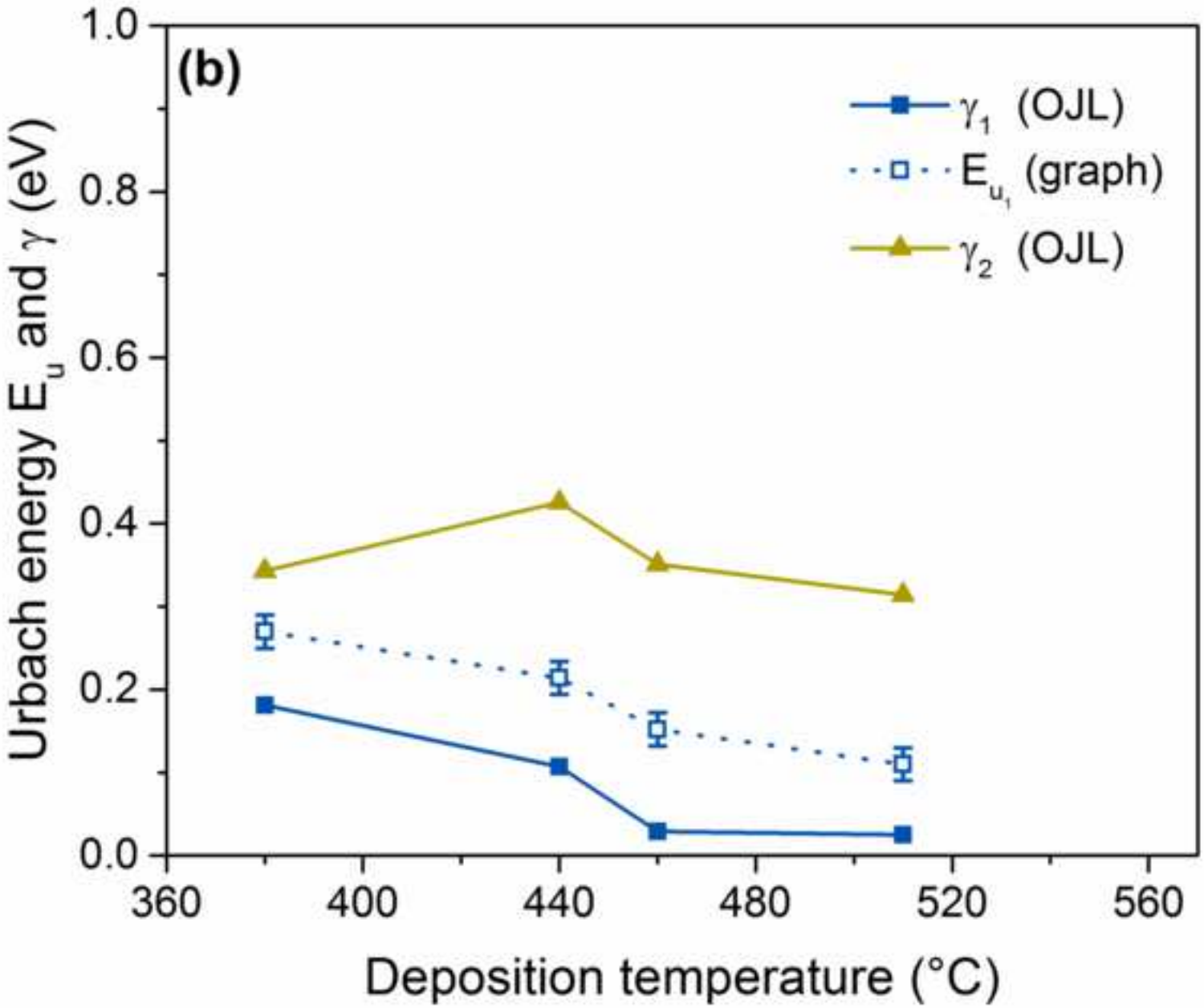

Figure 7a

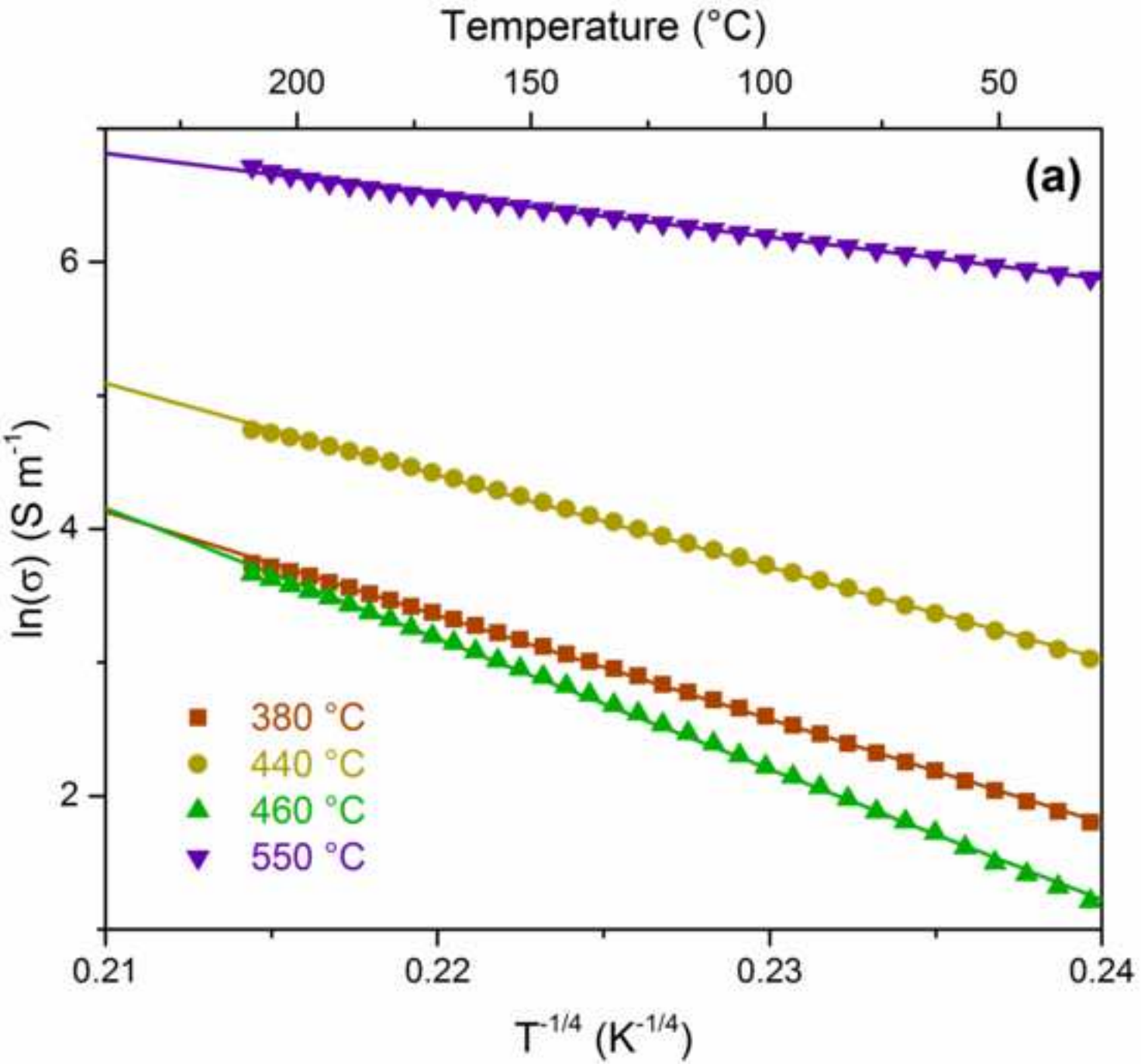

Figure 7b

Click here to access/download;Figure;Fig7b Hall conc vs mob a.tif

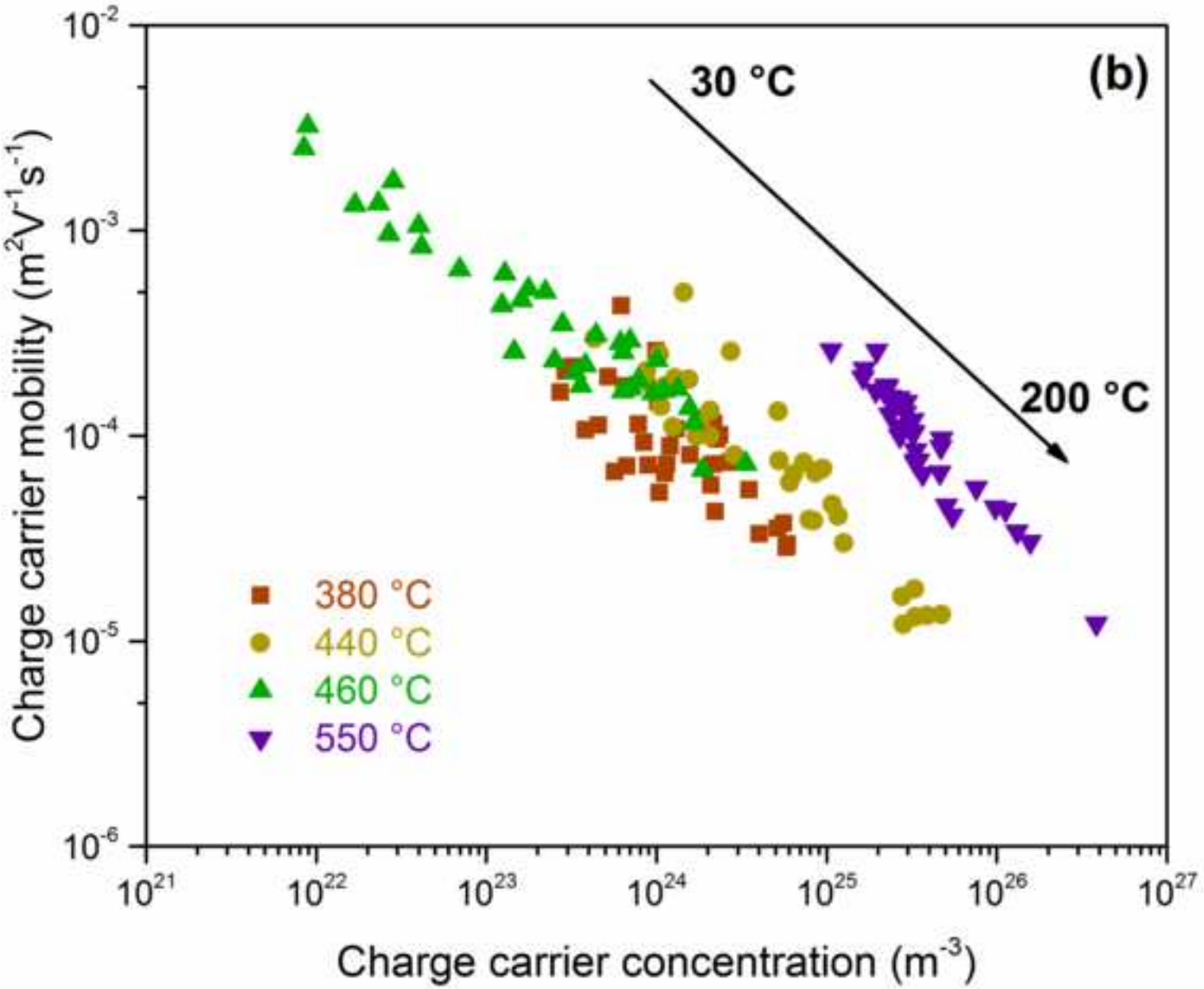

Figure 8a

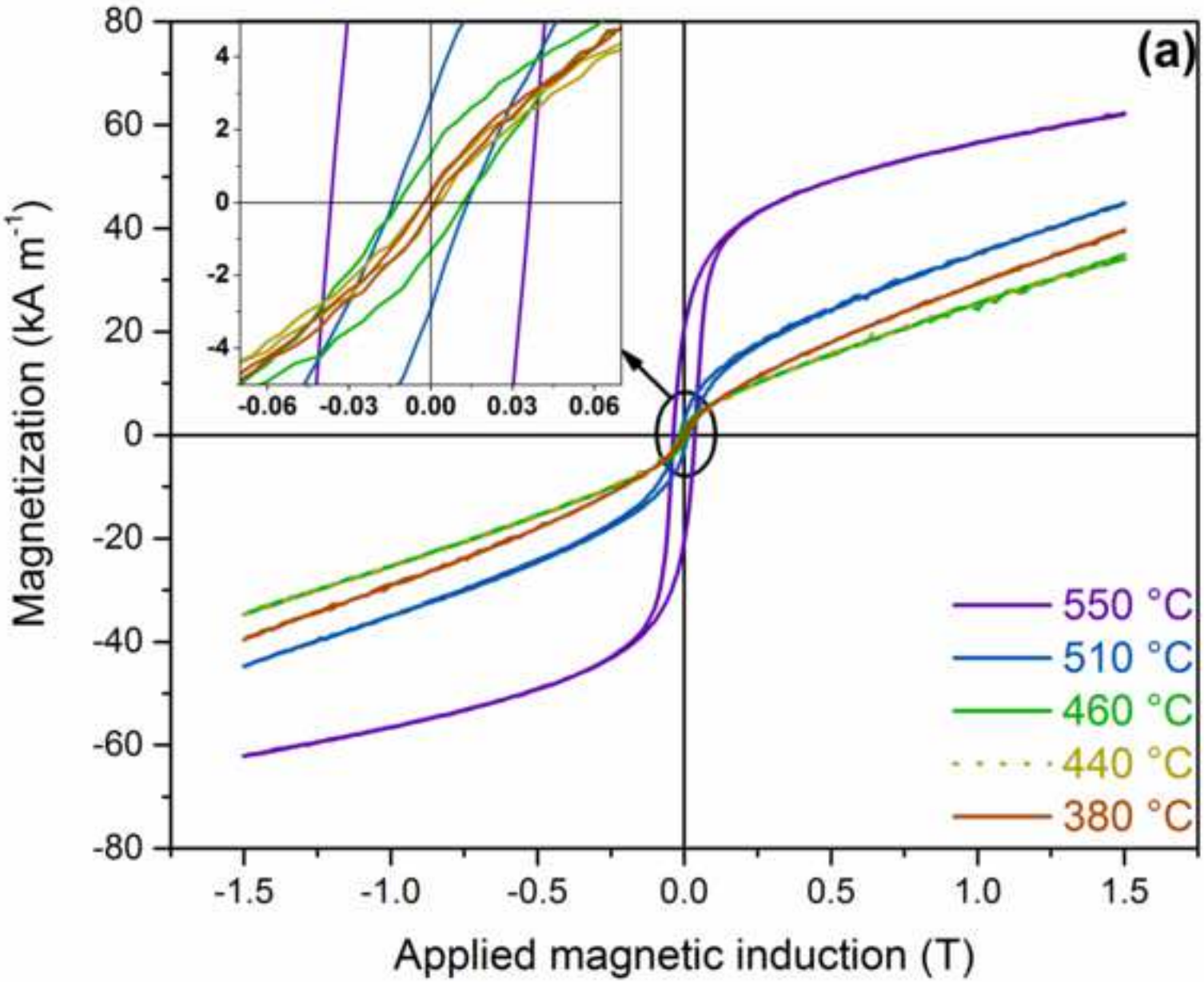

Figure 8b

Click here to access/download;Figure;Fig8b Magn values sans insert.tif